Check for updates

Three-dimensional NiCoP hollow spheres: an efficient electrode material for hydrogen evolution reaction and supercapacitor applications†

Jiban K. Das,[ab] Aneeya K. Samantara, [ID] [ab] Saumya Satyarthy,[ab] Chandra Sekhar Rout [ID] *[c] and J. N. Behera [ID] ⋆[ab]

A binary metal phosphide (NiCoP) has been synthesized in a single-step hydrothermal method, and its energy conversion (hydrogen evolution reaction; HER) and energy storage (supercapacitor) performances have been explored. The physicochemical characterization of the NiCoP nanostructures show that they have a highly crystalline phase and are formed uniformly with a sphere-like surface morphology. In acidic electrolytic conditions, the NiCoP shows excellent HER performance, requiring only 160 and 300 mV overpotential to deliver 10 and 300 mA cm^{-2} current density, respectively. Interestingly, it follows the Volmer–Heyrovsky reaction pathway to execute the HER with robust durability ($\sim$15 mV increase in overpotential even after 18 h of electrolysis). In an alkaline medium (5 M KOH), NiCoP shows specific capacitance of 960 F g^{-1} with higher energy density (33.3 W h kg^{-1}) and power density (11.8 kW kg^{-1}). Moreover, it shows better reversibility ($\sim$97% coulombic efficiency) and long cycle life ($\sim$95% capacitance retention after 10 000 repeated cycles). The unique surface morphology and phase purity of the binary metal phosphide avails more electroactive surface/redox centers, thereby showing better electrocatalytic as well as energy storage performances. Therefore, we presume that the NiCoP would be a suitable material for future energy conversion and storage systems.

Introduction

After many revolutionary evolutions in the energy sector, molecular hydrogen has been assumed as a greener and efficient fuel to substitute traditional fossil fuels.[1,2] Though it can be generated by following steam methane reforming, biomass electrolysis, natural gas oxidation, carbonation, and photo/electrochemical splitting of water, the electrochemical splitting of water (hydrogen evolution reaction; HER) remains the key emerging method for the qualitative and quantitative production of H$_2$ in a cost-effective manner.[3] The process generally depends on the active electrocatalyst that catalyzes the reduction of water at a lower overpotential.[4] In this regard, noble metal nanostructures, transition-metal-based nanostructures, and composites with various carbon materials have been explored.[5,6] However, noble-metal-based electrode materials still occupy the dominant position, but their scarce availability and high cost compel the research community to find suitable substitutes. Recently, different transition metal phosphides (TMPs) have been synthesized and are considered to represent promising electroactive materials to substitute noble-metal-based electrocatalysts.[7] In these cases, the phosphorous atom (P) plays a vital role in the catalytic performance improvement. Here, the higher electronegative nature of the phosphorous atom facilitate the withdrawal of electrons from the transition metal surface and traps the positively charged protons efficiently during the course of HER.[3,8,9] The synergistic effect of the multivalent transition metal sites (as hydride-acceptor centers) and the proton-acceptor phosphorous site of the TMPs promotes the HER. The P content in these TMPs proportionally increases the HER activity, but after a certain limit the activity decreases. Therefore, an optimized ratio of metal to phosphorous is strictly required to execute the HER efficiently.[10–12] Recently, various TMPs (Ni$_x$P, FeP, CoP, NiCoP, MoP, WP$_2$, etc.) have been developed following different synthesis methods and their HER activity studied in acidic as well as alkaline media.[13–19]

On the other hand, energy storage systems have equal importance for the smooth running of many electronics at the time of requirement. Although metal ion batteries have been broadly studied and high energy densities have been achieved, they are associated with a very low power density and cycle life. This creates a huge byproduct in a short span of time and

[a]National Institute of Science Education and Research (NISER), Khordha 752050, Odisha, India. E-mail: jnbehera@niser.ac.in

[b]Homi Bhabha National Institute, (HBNI), Mumbai, India

[c]Centre for Nano and Material Sciences, Jain University, Jain Global Campus, Ramanagaram, Bangalore 562112, India. E-mail: r.chandrasekhar@jainuniversity.ac.in

pollutes the environment. Therefore, alternative energy storage systems termed as supercapacitors/ultra-capacitors have been explored recently that have ultrahigh power density and nearly a 100-fold higher cycle life compared to batteries.[20,21] Moreover the hybrid storage system (integration of a supercapacitor with a battery) increases the life span of batteries. In this regard, various nanostructures of metal chalcogenides, metal oxides, hydroxides, graphene, activated carbon, and composite materials have been explored.[22,23] However, still the development of an active material with better charge-storage performance is required. Many metal-phosphide-based electrode materials have been explored that have shown either HER or supercapacitor activities, but a single metal phosphide showing both applications remains rare.

In this work, nickel–cobalt-based binary metal phosphide (NiCoP) in the form of three-dimensional (3D) hollow spheres has been synthesized following a single-step hydrothermal method. After systematic physicochemical characterizations, the electrocatalytic (HER) and charge-storage (supercapacitor) performance of the NiCoP have been explored in a two-compartment three-electrode electrochemical cell. The rough surface and hollow nature of the binary metal phosphide availed huge redox active centers, thereby facilitating the electrocatalysis as well as charge-transfer process. Moreover, the synergistic effect of Ni and Co with the phosphorous centers increased the electrical conductivity, leading to a superior rate capability. The NiCoP-modified electrode required only 160 mV overpotential to deliver the state-of-the-art current density (10 mA cm^{-2}) and followed the Volmer–Heyrovsky reaction pathway (with a Tafel slope of 70 mV dec^{-1}) to evolve hydrogen in an acidic medium. However, in an alkaline medium, the NiCoP-modified electrode showed a specific capacitance of 960 F g^{-1} with an energy density of 33.3 W h kg^{-1}, as well as an ultrahigh power density (11.8 kW kg^{-1}) and excellent cyclic stability (95% capacitance retention after 10 000 charge–discharge cycles). These observations clearly demonstrated that the as-developed binary metal phosphide is a promising electroactive material for future energy conversion and storage systems.

Experimental

Materials

Nickel(II) chloride hexahydrate, cobalt(II) chloride hexahydrate, and Nafion were purchased from Sigma-Aldrich, red phosphorous and potassium hydroxide (KOH) were purchased from Spectrochem. Deionized water was used for all solution preparations throughout the work.

Synthesis of NiCoP

The synthesis of bimetallic nickel cobalt phosphide (NiCoP) was carried out following a simple hydrothermal method. In particular, nickel(II) chloride hexahydrate (0.237 g) and cobalt(II) chloride hexahydrate (0.144 g) were mixed with 15 ml deionized water under stirring. Then, 0.54 g of red phosphorous and 0.56 g of KOH were added to the reaction precursor and left to stir for 1 h. The whole reaction mixture was transferred to a 23 ml Teflon-lined stainless steel autoclave and placed in a hot air oven at 200 °C for 24 h. After cooling down, the whole precipitate was collected, washed several times with deionized water as well ethanol, then dried in a hot air oven 60 °C and stored for further use.

Characterization

The crystal structure and phase purity of the sample were verified by powder X-ray diffraction system (Bruker D8 Advance diffractometer) equipped with Cu-Kα radiation ($\lambda = 1.5418$ Å). The surface morphology of NiCoP was studied with field emission scanning electron microscopy (FESEM, Merlin Compact with a GEMINI-I electron column, Zeiss Pvt. Ltd., Germany) and high-resolution transmission electron microscopy (HRTEM, JEOL 2100F, operated at 200 kV). A dilute dispersion of the sample was prepared in a mixture of ethanol/water and drop-cast onto a carbon-coated copper grid (200 mesh) and dried properly under a lamp prior to the HRTEM analysis. Further, elemental mapping was carried out to verify the elements present in the samples.

Electrochemical measurements

All the electrochemical measurements were performed in a two-compartment three-electrode electrochemical cell by a computer-controlled Bio-Logic Electrochemical workstation (EC-Lab, VSP 200). Here, a sample-cast glassy carbon electrode, bare platinum wire, and aqueous Ag/AgCl were taken as the working, auxiliary, and reference electrodes, respectively. For the hydrogen evolution reaction, 0.5 M H$_2$SO$_4$ was taken as the electrolyte, and linear sweep voltammograms were recorded at a sweep rate of 5 mV s^{-1}. The electrocatalyst ink was prepared by mixing 1 mg of NiCoP in a mixture of ethanol (95 μl) and Nafion (5 μl) followed by ultrasonication using a bath sonicator. Then, 5 μl of the ink was drop-cast onto well-polished (repeatedly polished with the slurry of 1, 0.3, and 0.05 μm of Al$_2$O$_3$ sequentially) glassy carbon electrode and dried in vacuum desiccator prior to the measurement. The LSVs were recorded in aqueous Ag/AgCl reference electrode and presented here *versus* the reversible hydrogen electrode (RHE) as per the following Nernst equation:[24–26]

$$E_{RHE} = E_{Ag/AgCl} + 0.059 \text{ (pH)} + E^0_{Ag/AgCl} \quad (1)$$

where, $E^0_{Ag/AgCl}$ is the standard potential of Ag/AgCl, *i.e.*, 0.21 V. Electrochemical impedance spectroscopy (EIS; Nyquist impedance) measurements were recorded in a potentiostatic mode at −0.25 V (*vs.* RHE) with an AC amplitude of 10 mV in the frequency range of 1 MHz to 0.1 Hz. Further *iR* compensation was performed to eliminate the catalyst and electrolyte resistance and to achieve the intrinsic catalytic performances of the electrode. Here, "*R*" is the uncompensated solution resistance that was obtained from the Nyquist plot and "*i*" is the observed current. The Tafel slopes were obtained by fitting the linear portion of the Tafel plot (plot of log *J* vs. overpotential) as per the following equation:[3,25]

$$\eta = a + b \log J \qquad (2)$$

where, a, b, η, and J are the Tafel constant, Tafel slope, overpotential, and current density. The electrochemical energy storage (supercapacitor) performance of the electrode material was evaluated by recording the cyclic voltammograms (at different sweep rates) and the galvanostatic charge–discharge (at different applied current densities) in 5 M KOH electrolyte. The preparation of working electrode remained the same as discussed above.

Results and discussion

NiCoP was synthesized by a single-step hydrothermal method using nickel(II) chloride hexahydrate, cobalt(II) chloride hexahydrate and red phosphorous as discussed in the experimental section. After synthesis, the crystallinity and purity of the sample were verified by powder X-ray diffraction analysis (Fig. 1), in which it showed a very sharp diffraction pattern and the observed hkl values [(111), (201), (210), (300), (002), (211), (212)] could be indexed to the hexagonal crystal structure of NiCoP (JCPDS no. 01-071-2336). Further, no additional peaks were observed, indicating the high phase purity and crystalline nature of the as-synthesized sample.

Thereafter, the surface morphology of NiCoP was verified by employing field-emission scanning electron microscopy and transmission electron microscopy (Fig. 2a–d). The NiCoP particles had a hollow sphere-like morphology with an average diameter of 1 μm. Close analysis of these spheres revealed that initially nanoparticles of NiCoP were formed and then assembled to make such a sphere-like morphology during the course of the hydrothermal reaction.

Therefore, the surface was observed to be very much roughened. The hollow and roughened surface of the nanostructures availed more electroactive centers, thereby providing better electrocatalytic performance for HER as well as better charge-storage performance for supercapacitors. Further, the selected area electron diffraction (SAED) pattern and well-defined fringes showed the crystalline nature of the sample, agreeing with the above-discussed PXRD pattern (Fig. 2e and f and S1†). Also, inter-planar lattice spacing of 0.217 nm was observed, corresponding to the [111] plane of NiCoP. The EDS elemental mapping obtained from the TEM analysis clearly indicated the uniform distribution of Ni, Co, and P in the as-synthesized NiCoP (Fig. S2†).
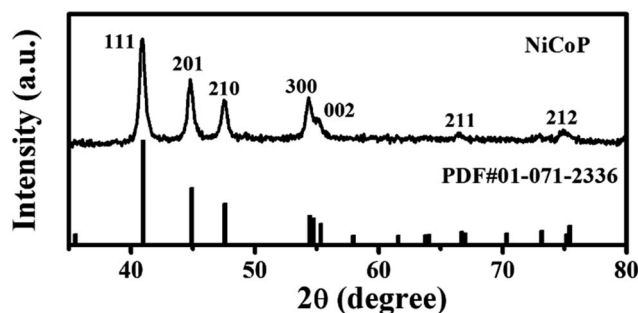

Fig. 1 Powder X-ray diffraction analysis of NiCoP.

The electrochemical hydrogen evolution reaction was carried out in a two-compartment three-electrode electrochemical cell with 0.5 M H_2SO_4 electrolyte. The linear sweep voltammetry was performed with the NiCoP and commercial Pt/C and the results are presented in Fig. 3a. The LSVs of NiCoP and Pt/C before and after iR correction are presented in Fig. S3 of the ESI.† It can be seen that the NiCoP catalyzed the HER efficiently, requiring only 160 and 300 mV overpotentials to deliver 10 and 300 mA cm^{-2} current densities, respectively. These values were observed to be favorably less in comparison to the catalytic behavior of other transition-metal-based HER electrocatalysts.[27–30] In order to analyze the impact of platinum wire (as a counter electrode) in the HER activity of NiCoP, we performed the HER experiment using graphite rod as a counter electrode under similar electrolytic conditions and the results are presented in Fig. S4.† Here no such change in the HER performance of NiCoP was noticed. Further the reaction kinetics of the NiCoP for HER was accessed from the Tafel slope calculated from the Tafel plot (plot of the log of the current density *versus* the overpotential).[31] For the commercial Pt/C and NiCoP, the observed Tafel slopes were 32 and 70 mV dec^{-1}, respectively. These illustrated that a Volmer–Tafel and Volmer–Heyrovsky reaction pathway might be followed by the Pt/C and NiCoP to execute HER (Fig. 3b).[3,4,32] Electrochemical impedance spectroscopy (EIS) was carried out in a frequency range of 1 MHz to 0.1 Hz and the results presented as a Nyquist impedance spectrum (plot of imaginary *vs.* real impedance) in Fig. 3c. The EIS spectrum was fitted with the corresponding Randles circuit (inset of Fig. 3c), which constitutes the series resistance (R_S; originating from the resistance of the solution, connectors *etc.*), charge-transfer resistance (R_{CT}; resistance for the transfer of charges among the current collector and electrode material), and a double-layer capacitor (C_{dl}).[33,34] From the literature study it is well known that for an efficient electrode material, the values of R_S and R_{CT} should be at a minimum. These values were obtained by simulating the experimental data using the Ec-Lab software of Biologic Instruments. It was observed that the R_S and R_{CT} values for the NiCoP were 5.1 and 7.04 Ω, respectively.

This observation clearly supported the favorable HER kinetics and excellent electron transport in the binary metal phosphide electrode material. Further, the durability of the electrode material for the electrocatalysis was monitored using the chronopotentiometry technique at the state-of-the-art current density (10 mA cm^{-2}). Interestingly, the NiCoP showed a negligible hike in overpotential (15 mV) even after 18 h of electrolysis (Fig. 3d). Again, in order to verify the impact of platinum counter electrode in the HER performance, the durability test of the electrode material was performed using graphite rod (as the counter electrode) and the results are presented in Fig. S5.† An increase in overpotential of 22 mV was observed even after 18 h of electrolysis, which was very close to that recorded previously using the bare Pt wire counter electrode. This observation clearly signified the non-interference of the Pt wire counter during the HER. Moreover, the robustness of the electrocatalyst was supported by analyzing the post stability sample by FESEM and PXRD patterns, as presented in Fig. 4. No such phase transformation and morphology change was
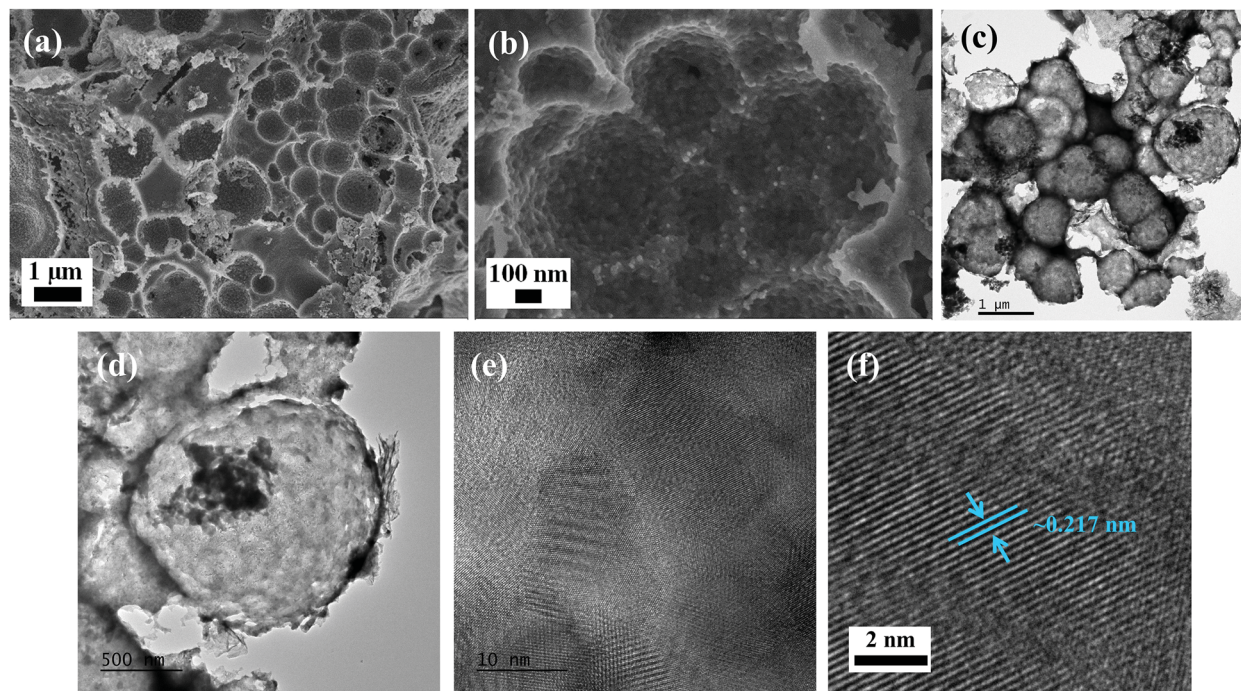
Fig. 2 (a and b) Field-emission scanning electron microscope images, (c–f) transmission electron microscopic images for the NiCoP at different magnifications.

observed, revealing the excellent durability of the NiCoP for long-term electrolysis. The electrocatalytic performance of the NiCoP was compared with other reported cathode electrode materials, as presented in Table S1 of the ESI.†

Thereafter the electrochemical energy storage performance of the NiCoP was verified in a two-compartment three-electrode electrochemical cell using 5 M KOH electrolyte. The detailed electrode preparation is presented in the experimental section.

First, the cyclic voltammograms at various sweep rates (1, 2, 4, 8, 10, 20, 40, 80, 100 mV s^{-1}) were recorded and are presented in Fig. 5a. Because of the reversible valence change between Co^{2+}/Co^{3+} and Ni^{2+}/Ni^{3+}, two distinct redox peaks were observed in all the CV profiles. Moreover, on increasing the sweep rate, a positive shift in the oxidation peak and a negative shift of the reduction peak position were observed.[35] This behavior could be ascribed to the polarization effect of the electrode at higher sweep rates in all the CV curves.[36,37] Further, the galvanostatic charge–discharge (GCD) profiles of the sample were recorded at various applied current densities, as seen in Fig. 5b. The specific capacitance (C_s) shown by the binary metal phosphide was evaluated from the CV (eqn (3)) and GCD (eqn (4)) profiles using the following equation:[26,37]

$$C_s = \frac{\int I \, dv}{2[m\theta(\Delta V)]} \quad (3)$$

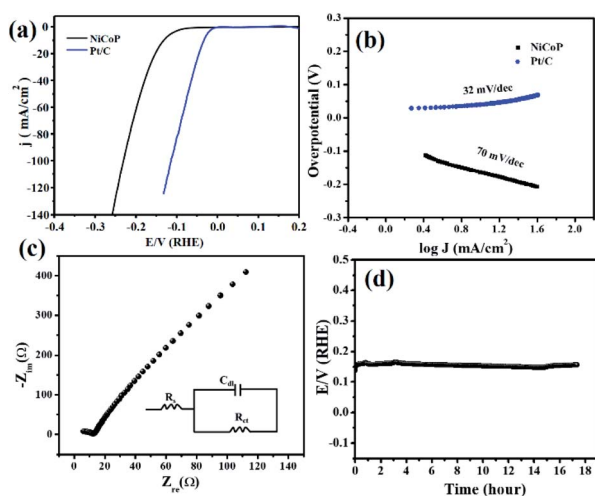$$C_s = \frac{I\Delta t}{m\Delta V} \quad (4)$$

Fig. 3 (a) Linear sweep voltammogram and (b) corresponding Tafel plot of NiCoP and Pt/C, (c) Nyquist impedance spectrum and (d) long-term stability test for HER at a 10 mA cm^{-2} current density in 0.5 M H$_2$SO$_4$. The LSV was recorded at a sweep rate of 5 mV s^{-1}. Inset of (c) is the Randles circuit diagram.
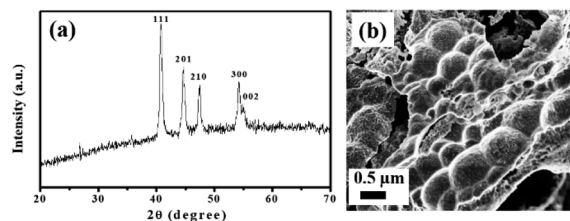

Fig. 4 (a) PXRD and (b) FESEM image of NiCoP after electrolysis for 18 h in 0.5 M H$_2$SO$_4$ at a 10 mA cm^{-2} current density.

where, $\int I dv$, m, θ, ΔV, I, Δt are the area under the CV curve, mass of the active electrode material, sweep rate, potential window, applied current, and discharge time, respectively. The NiCoP showed specific capacitances of 960, 800, 630, 460, 380, 262, 183, 146, and 132 F g^{-1} at 1, 2, 4, 8, 10, 20, 40, 80, and 100 mV s^{-1} sweep rates. It is well known that the specific energy (ED) and specific power (PD) are two main parameters of an energy storage system to evaluate their efficacy for practical application. Therefore, the ED and PD were calculated from the C_s values as per the following equations:[37]
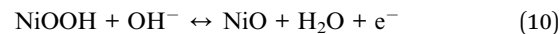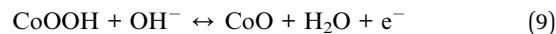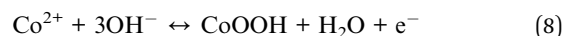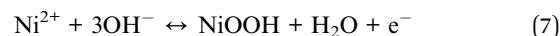
$$ED = \frac{C_s (\Delta V)^2}{2} \quad (5)$$

$$PD = \frac{C_s (\Delta V)\theta}{2} \quad (6)$$

Interestingly, the NiCoP showed a specific energy of 33.3 W h kg^{-1} and specific power of 11.8 kW kg^{-1}. These values were observed to be high in comparison to the recently reported single and binary metal phosphides, *etc.* In a particular work, Cheng *et al.* observed a specific capacitance of 284 F g^{-1} and 416 F g^{-1} for Co$_2$P nanorods and nanoflowers, respectively.[38] By following a two-step synthesis method (ball milling followed by annealing), Wang *et al.* prepared Ni$_2$P and Ni$_5$P$_4$ and observed specific capacitances of 843.25 and 801.5 F g^{-1}, respectively.[39] In another work, Yang's group prepared a Ni, Co binary metal phosphide (NiCoP) and obtained a specific capacitance of 646 F g^{-1}.[40] A performance comparison of the NiCoP with other reported material is provided in Table S2 of the ESI.† Moreover, the NiCoP showed a reversible charging–discharging process with a coulombic efficiency of ∼97% and ∼95% retention of the initial capacitance even after 10 000 repeated cycles. The excellent reversibility and robust stability suggest the binary metal phosphide is a suitable material for future energy storage systems. Further, the post stability sample was collected and their surface morphology and phase transformation were analyzed using PXRD and FESEM (Fig. 6).

It was revealed that NiCoP was partially transformed to the corresponding metal oxide and oxy hydroxide during the course of the charging–discharging process. This *in situ* transformation of NiCoP to NiO (PDF#01-089-7101), CoO (PDF#01-089-2823), and NiO(OH) (PDF#00-059-0464) could be clearly seen from the lattice fringes obtained from the HRTEM images and the corresponding SAED pattern (Fig. S6†). However, no such prominent change in the surface morphology was noticed. This phase transformation was presumed to be due to the treatment of the binary metal phosphide in the higher alkaline condition.

During the course of the charge–discharge measurement in the alkaline electrolytic condition, the surface of the loaded electrode material was partially oxidized. Therefore, the Ni and Co cations present on the NiCoP surface get oxidized to form NiO, CoO, NiO(OH), *etc.* as per the following equations and they remain as NiCoP/NiO NiCoP/CoO, and NiCoP/NiO(OH) as active centers.[41–43]

$$Ni^{2+} + 3OH^- \leftrightarrow NiOOH + H_2O + e^- \quad (7)$$

$$Co^{2+} + 3OH^- \leftrightarrow CoOOH + H_2O + e^- \quad (8)$$

$$CoOOH + OH^- \leftrightarrow CoO + H_2O + e^- \quad (9)$$

$$NiOOH + OH^- \leftrightarrow NiO + H_2O + e^- \quad (10)$$

Here the synergistic effect of both the phosphide and oxide surface plays a vital role in the improvement of the charge-storage performance. After careful analysis of the post stability sample, we observed the surface of the NiCoP was oxidized during the course of stability measurement. In this case, the charge storage takes place because of the pseudocapacitive behavior of the *in situ* surface-oxidized NiCoP. During
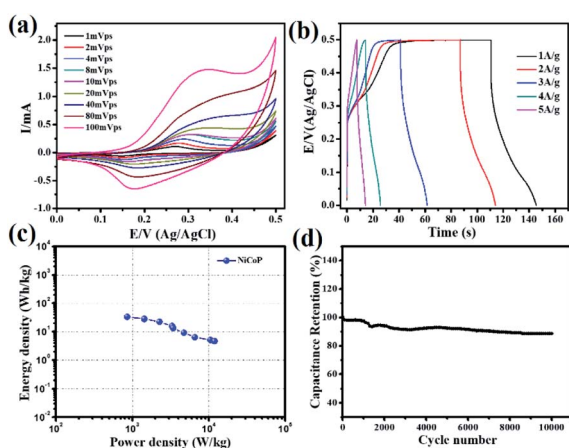

Fig. 5 (a) Cyclic voltammograms at different sweep rates, (b) galvanostatic charge−discharge profiles at various applied current densities, (c) corresponding Ragone plot, and (d) plot of the cyclic stability for the NiCoP-modified electrode in 5 M KOH electrolyte.
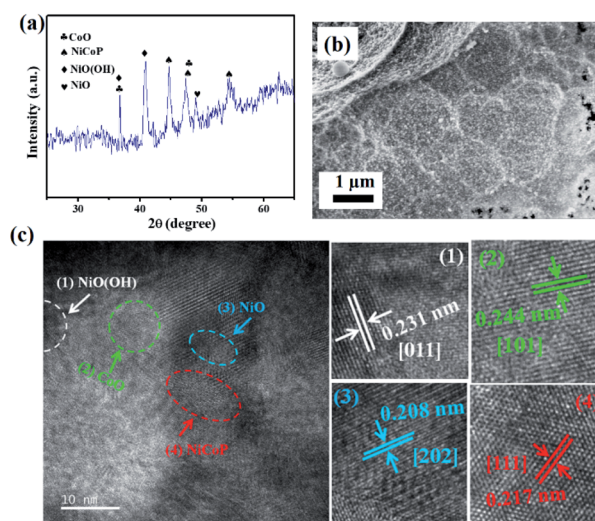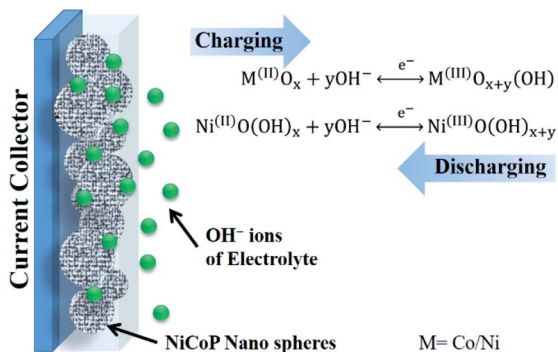

Fig. 6 (a) PXRD, (b) FESEM, and (c) HRTEM images of NiCoP after 10 000 repeated cycles in 5 M KOH electrolyte.

Scheme 1 Scheme showing the charge–discharge process of the surface-oxidized NiCoP in alkaline electrolyte (5 M KOH).

the charging process (anodic scan of the cyclic voltammogram), surface oxidation takes place, transforming Ni^{2+} to Ni^{3+} and Co^{2+} to Co^{3+}. However during discharge, a reduction in the oxidation state takes place (Scheme 1).

These couple of reactions occur on the oxidized surface of the NiCoP electrode and enable the system to store charge efficiently in alkaline medium. The electrocatalytic (for HER) and electrochemical energy storage (supercapacitor) performances of the NiCoP could be due to the combined effects of its unique surface morphology and crystallinity, better electrochemical conductivity, and phase purity. Therefore, it is presumed that this binary metal phosphide can be used as an efficient electrode material for future energy conversion and storage systems.

Conclusions

In this work, by using a single-step hydrothermal method, the scalable synthesis of a binary metal phosphide (NiCoP) has been presented. The NiCoP had a highly crystalline sphere-like morphology and the particles were uniformly formed with higher phase purity. Further, the as-synthesized NiCoP was used as an electrode material for electrocatalysis (toward HER) and energy storage (supercapacitor) applications. It required only 160 mV of overpotential to deliver the state-of-the-art current density (10 mA cm^{-2}) and followed the Volmer–Heyrovsky reaction pathway for the evolution of hydrogen. Further, it showed excellent electrochemical charge-storage performance with a specific capacitance of 960 F g^{-1} together with a specific energy and specific power of 33.3 W h kg^{-1} and 11.8 kW kg^{-1}, respectively. Interestingly, this binary metal phosphide showed robust durability during both electrolysis (15 mV increase in overpotential after 18 h of electrolysis) and charge–discharge (~95% capacitance retention). This excellent durability during electrocatalysis as well as its charge-storage performance suggest that NiCoP would be an efficient material for future energy conversion and storage systems.

Conflicts of interest

There are no conflicts to declare.

Acknowledgements

Notes and references

1 J. O. Bockris, *Int. J. Hydrogen Energy*, 2002, **27**, 731–740.
2 M. D. Leonard, E. E. Michaelides and D. N. Michaelides, *Renewable Energy*, 2020, **145**, 951–962.
3 A. K. Samantara and S. Ratha, *Metal Oxides/Chalcogenides and Composites*, Springer International Publishing, 1st edn, 2019, pp. XVII–83.
4 S. Anantharaj, S. R. Ede, K. Sakthikumar, K. Karthick, S. Mishra and S. Kundu, *ACS Catal.*, 2016, **6**, 8069–8097.
5 G. Zhao, K. Rui, S. X. Dou and W. Sun, *Adv. Funct. Mater.*, 2018, **28**, 1803291.
6 S. Sarkar and S. C. Peter, *Inorg. Chem. Front.*, 2018, **5**, 2060–2080.
7 Y. Wang, B. Kong, D. Zhao, H. Wang and C. Selomulya, *Nano Today*, 2017, **15**, 26–55.
8 P. Liu and J. A. Rodriguez, *J. Am. Chem. Soc.*, 2005, **127**, 14871–14878.
9 Y. Liu, H. Cheng, M. Lyu, S. Fan, Q. Liu, W. Zhang, Y. Zhi, C. Wang, C. Xiao, S. Wei, B. Ye and Y. Xie, *J. Am. Chem. Soc.*, 2014, **136**, 15670–15675.
10 J. F. Callejas, C. G. Read, E. J. Popczun, J. M. McEnaney and R. E. Schaak, *Chem. Mater.*, 2015, **27**, 3769–3774.
11 Y. Pan, Y. Liu, J. Zhao, K. Yang, J. Liang, D. Liu, W. Hu, D. Liu, Y. Liu and C. Liu, *J. Mater. Chem. A*, 2015, **3**, 1656–1665.
12 P. E. R. Blanchard, A. P. Grosvenor, R. G. Cavell and A. Mar, *Chem. Mater.*, 2008, **20**, 7081–7088.
13 X. Li, L. Jiang, J. Liu, Q. Hua, E. Wang and G. Xie, *J. Energy Chem.*, 2020, **43**, 121–128.
14 Y. Lin, Y. Pan, S. Liu, K. Sun, Y. Cheng, M. Liu, Z. Wang, X. Li and J. Zhang, *Appl. Catal. B Environ.*, 2019, **259**, 118039.
15 J. Jiang, C. Wang, J. Zhang, W. Wang, X. Zhou, B. Pan, K. Tang, J. Zuo and Q. Yang, *J. Mater. Chem. A*, 2015, **3**, 499–503.
16 M. Pi, T. Wu, D. Zhang, S. Chen and S. Wang, *Nanoscale*, 2016, **8**, 19779–19786.
17 P. Jiang, Q. Liu and X. Sun, *Nanoscale*, 2014, **6**, 13440–13445.
18 X. Zhang, X. Yu, L. Zhang, F. Zhou, Y. Liang and R. Wang, *Adv. Funct. Mater.*, 2018, **28**, 1706523.
19 A. Dutta, A. K. Samantara, S. K. Dutta, B. K. Jena and N. Pradhan, *ACS Energy Lett.*, 2016, **1**, 169–174.
20 J. Yan, Q. Wang, T. Wei and Z. Fan, *Adv. Energy Mater.*, 2014, **4**, 1300816.
21 P. Simon, Y. Gogotsi and B. Dunn, *Science*, 2014, **343**, 1210–1211.

22 A. K. Samantara and S. Ratha, *Materials development for Active/Passive components of a supercapacitor: background, present status and future perspective*, Springer Singapore, 1st edn, 2018, pp. XI–48.

23 N. S. A. Manaf, M. S. A. Bistamam and M. A. Azam, *ECS J. Solid State Sci. Technol.*, 2013, **2**, M3101–M3119.

24 R. K. Tripathy, A. K. Samantara and J. N. Behera, *Dalton Trans.*, 2019, **48**, 10557–10564.

25 J. K. Das, A. K. Samantara, A. K. Nayak, D. Pradhan and J. N. Behera, *Dalton Trans.*, 2018, **47**, 13792–13799.

26 A. K. Samantara, S. Kamila, A. Ghosh and B. K. Jena, *Electrochim. Acta*, 2018, **263**, 147–157.

27 Q. Liu, J. Tian, W. Cui, P. Jiang, N. Cheng, A. M. Asiri and X. Sun, *Angew. Chem. Int. Ed.*, 2014, **53**, 6710–6714.

28 Y. Xu, R. Wu, J. Zhang, Y. Shi and B. Zhang, *Chem. Commun.*, 2013, **49**, 6656–6658.

29 A. Lu, Y. Chen, H. Li, A. Dowd, M. B. Cortie, Q. Xie, H. Guo, Q. Qi and D. L. Peng, *Int. J. Hydrogen Energy*, 2014, **39**, 18919–18928.

30 J. Lin, Z. Peng, G. Wang, D. Zakhidov, E. Larios, M. J. Yacaman and J. M. Tour, *Adv. Energy Mater.*, 2014, **4**, 1301875.

31 S. A. Vilekar, I. Fishtik and R. Datta, *J. Electrochem. Soc.*, 2010, **157**, B1040–B1050.

32 B. E. Conway and B. V Tilak, *Electrochim. Acta*, 2002, **47**, 3571–3594.

33 Y. Zhang, B. Ouyang, J. Xu, S. Chen, R. S. Rawat and H. J. Fan, *Adv. Energy Mater.*, 2016, **6**, 1600221.

34 D. Hou, W. Zhou, X. Liu, K. Zhou, J. Xie, G. Li and S. Chen, *Electrochim. Acta*, 2015, **166**, 26–31.

35 T. Dang, L. Wang, D. Wei, G. Zhang, Q. Li, X. Zhang, Z. Cao, G. Zhang and H. Duan, *Electrochim. Acta*, 2019, **299**, 346–356.

36 J. Park, T. H. Ko, S. Balasubramaniam, M.-K. Seo, M.-S. Khil, H. Y. Kim and B. S. Kim, *Ceram. Int.*, 2019, **45**, 13099–13111.

37 J. K. Das, A. K. Samantara, K. A. Sree Raj, C. S. Rout and J. N. Behera, *Dalton Trans.*, 2019, **48**, 15955–15961.

38 X. Chen, M. Cheng, D. Chen and R. Wang, *ACS Appl. Mater. Interfaces*, 2016, **8**, 3892–3900.

39 D. Wang, L.-B. Kong, M.-C. Liu, Y.-C. Luo and L. Kang, *Chem.–Eur. J.*, 2015, **21**, 17897–17903.

40 C. Wang, Y. Qian, J. Yang, S. Xing, X. Ding and Q. Yang, *RSC Adv.*, 2017, 7, 26120–26124.

41 A. Gopalakrishnan, D. Yang, J. C. Ince, Y. B. Truong, A. Yu and S. Badhulika, *Journal of Energy Storage*, 2019, **25**, 100893.

42 R. Ding, X. Li, W. Shi, Q. Xu and E. Liu, *Chem. Eng. J.*, 2017, **320**, 376–388.

43 W. Wei, L. Mi, Y. Gao, Z. Zheng, W. Chen and X. Guan, *Chem. Mater.*, 2014, **26**, 3418–3426.